Article

Nonlocality-enabled photonic analogies of parallel spaces, wormholes and multiple realities

Tongtong Song[1,6], Yongxin Jing[1,6], Changhui Shen[1,6], Hongchen Chu[2], Jie Luo [3], Runqi Jia[1], Cong Wang[1], Meng Xiao [4], Zhao-Qing Zhang[5], Ruwen Peng [1]✉, Mu Wang [1]✉, C. T. Chan [5]✉ & Yun Lai [1]✉

The concepts of the multiverse and wormholes in dimensions beyond our physical space have long captivated curiosity and imagination, yet experimental demonstrations remain elusive. In this work, we employ nonlocal artificial materials to construct a photonic analogy of parallel spaces, where two distinct effective optical media coexist within a single artificial material, each accessible through different material boundaries. Enhanced by deep learning, this method further enables the analogies of two fascinating phenomena: photonic wormholes as invisible optical tunnels, and photonic multiple realities, where two different optical devices or scatterers function independently at the same location as if they exist in separate dimensions. Our findings empower optical designs to transcend the limitations of physical dimensions effectively, paving the way for an unprecedented degree of freedom in multiplexing.

The multiverse, or parallel universes[1]—often envisioned as alternate realities coexisting independently within separate dimensions—has long captivated scientific thought and spurred discussions ranging from cosmology to science fiction. Concurrently, wormholes[2,3], hypothetical tunnels that connect distant points or different dimensions in space-time, have intrigued the public as potential shortcuts through the universe. Despite recent reports of holographically traversable wormholes in quantum computers[4], experimentally demonstrating these fascinating phenomena remains an elusive challenge due to the fundamental dimensional constraint of our physical space.

In recent decades, artificial optical materials—including metamaterials[5–8] and photonic crystals[9–12]—have enabled the discovery of numerous phenomena, such as photonic band gaps[9], topological photonics[13,14], bound states in the continuum[15–18], negative refraction and perfect lenses[19–21], invisibility and illusionary effects[22–33], zero-refractive-index photonics[34–37], effective gauge potential[38–40], synthetic dimensions[41,42] and hypothesized multiverses or parallel universes[43,44]. In this work, based on nonlocal artificial materials with multiple shifted dispersions, we introduce a mechanism that enables a single physical space to emulate two parallel spaces for photons, which are effectively described as two distinct optical media occupying the same physical space but accessible only through different boundaries. With the aid of deep learning[29,45], the properties of such photonic parallel spaces can be flexibly engineered. We demonstrate that this mechanism enables the photonic analogies of two fascinating phenomena: photonic wormholes as invisible optical tunnels with configurable effective refractive index for tunneling photons, and photonic multiple realities, where two arbitrary optical devices or scatterers occupy the same physical space while operating independently as if they exist in separate dimensions. The numerical and experimental results verified our

[1]National Laboratory of Solid State Microstructures, School of Physics, Collaborative Innovation Center of Advanced Microstructures and Jiangsu Physical Science Research Center, Nanjing University, Nanjing, China. [2]School of Physics and Technology, Nanjing Normal University, Nanjing, China. [3]School of Physical Science and Technology, Soochow University, Suzhou, China. [4]Key Laboratory of Artificial Micro- and Nano-structures of Ministry of Education and School of Physics and Technology, Wuhan University, Wuhan, China. [5]Department of Physics and Institute for Advanced Study, The Hong Kong University of Science and Technology, Kowloon, Hong Kong, China. [6]These authors contributed equally: Tongtong Song, Yongxin Jing, Changhui Shen. ✉e-mail: rwpeng@nju.edu.cn; muwang@nju.edu.cn; phchan@ust.hk; laiyun@nju.edu.cn

theory consistently. Our findings, although not actualizing the concepts of parallel spaces, wormholes, and multiple realities in reality, open a gateway to effectively emulate these phenomena based on nonlocal photonics, thereby bridging the significant gap between theoretical concepts and practical implementations for these higher-dimensional concepts.

Results

The concept and theory of photonic parallel spaces

The optical response of natural materials, such as a butterfly shown in Fig. 1a, can be characterized by a spatial distribution of optical parameters, e.g., the refractive index $n(x,y)$, corresponding to an optical space. So far, it is commonly believed that there is a one-to-one correspondence between the physical and optical spaces. Here, we demonstrate that the physical space occupied by a single artificial material can effectively correspond to two different optical spaces, such as a butterfly, $n_1(x,y)$ and a maple leaf, $n_2(x,y)$, simultaneously, as shown in Fig. 1b. Interestingly, these two optical spaces are only accessible through different boundaries of the artificial material, thus they function independently without mutual interaction. This phenomenon resembles the concept of parallel spaces or multiple realities for photons.

Figure 1c demonstrates three examples depicting the exciting possibilities endowed by this premise. In the left panel, an artificial material can simultaneously produce the scattering patterns of two arbitrary optical scatterers, e.g., a butterfly and a maple leaf. In the middle panel, an artificial material is simultaneously equivalent to two arbitrary optical media, such as those with refractive indices $n \approx 0$ and $n \approx 1$, merging the distinct signatures of angular filtering and free transmission. In the right panel, an artificial material integrates two arbitrary optical devices, e.g., a convex lens and a concave lens, in the same physical space, yet preserving both functionalities. The choice of these distinct optical realities is determined by the boundaries

(marked as red or blue) through which external photons enter the physical domain. An illustrative animation is provided in Supplementary Video 1.

The mechanism behind these amazing functionalities relies on a special form of nonlocality[46,47]: multiple dispersions shifted away from the Brillouin Zone center in different directions. To illustrate this concept, we first consider transverse electric (TE) electromagnetic waves (electric field along the z direction) propagating in the two-dimensional (2D) x–y plane. An ordinary anisotropic material characterized by the dispersion relation $k_x^2/\mu_y + k_y^2/\mu_x = \varepsilon_z k_0^2$ corresponds to a single optical space described by $(\varepsilon_z, \mu_x, \mu_y)$, where ε and μ are the relative permittivity and permeabilities. $\mathbf{k} = (k_x, k_y)$ is the wave vector, and k_0 is the wave number in free space. The equal-frequency contours (EFCs) in Fig. 2a show the elliptical equal-frequency surface of the material (solid ellipse) and the circular equal-frequency surfaces of free space (dashed circles) at a single operating frequency. Both of them are located at the Brillouin Zone center. The electromagnetic response of this material under illumination is determined by the coupling of the eigenstates inside and outside the material. Obviously, normal optical materials cannot function as photonic parallel spaces.

Now, envision an artificial material characterized by two dispersion relations shifted along the x and y directions near the operating frequency, which can be expressed as follows:

$$\frac{(k_x - k_\alpha)^2}{\mu_y^\alpha} + \frac{k_y^2}{\mu_x^\alpha} = \varepsilon_z^\alpha k_0^2 \tag{1a}$$

$$\frac{k_x^2}{\mu_y^\beta} + \frac{(k_y - k_\beta)^2}{\mu_x^\beta} = \varepsilon_z^\beta k_0^2 \tag{1b}$$

Here, k_α and k_β represent the constants of momentum shift in the x and y directions, respectively. This momentum shift implies a special
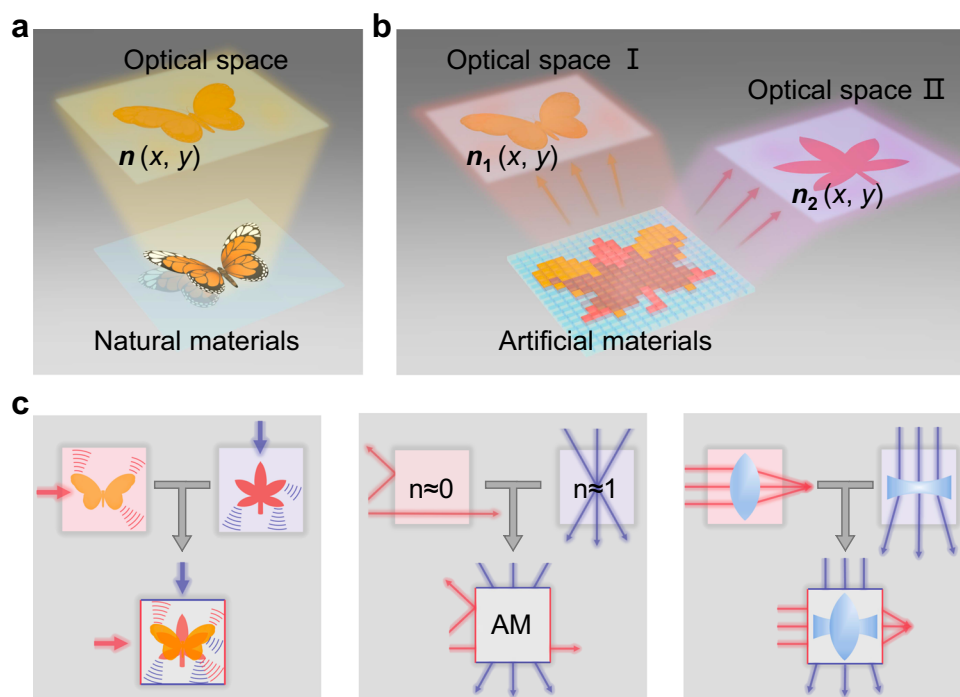
Fig. 1 | Concept of photonic parallel spaces and versatile functionalities. a A butterfly and its optical space characterized by refractive index distribution $n(x,y)$. **b** An artificial material (AM) with two different optical spaces, I and II, which correspond to two distinct refractive index distributions, $n_1(x,y)$ and $n_2(x,y)$, respectively. The choice of the optical space depends on the boundary through which external photons access the artificial material. **c** Schematic applications of photonic parallel spaces. The left, middle, and right panels demonstrate, respectively, three artificial materials with two distinct optical spaces, namely, a butterfly and a maple leaf as two distinct scatterers (left), two optical media of refractive index $n \approx 0$ and $n \approx 1$ (middle), and a convex lens and a concave lens (right).
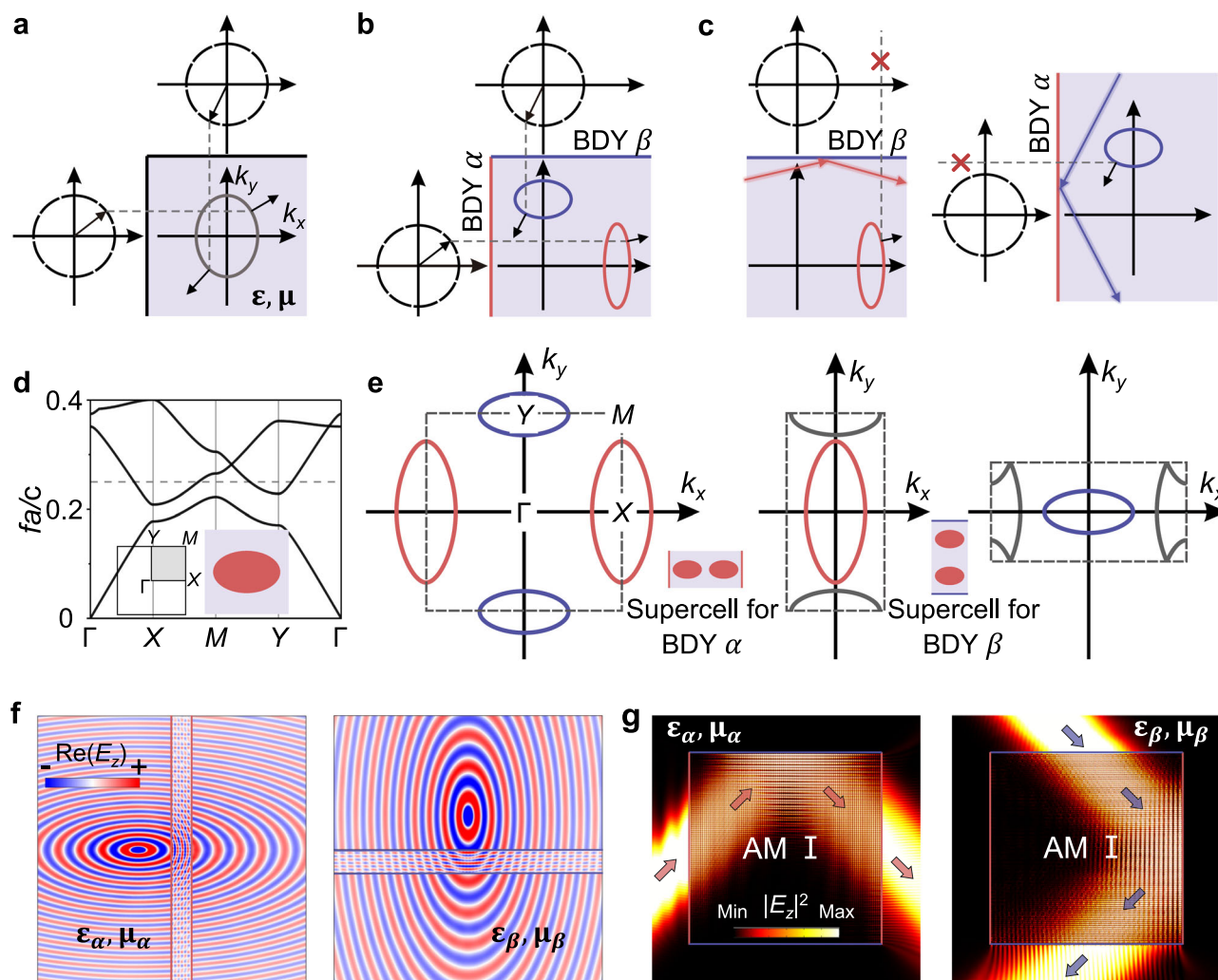
Fig. 2 | Principle of photonic parallel spaces. a The EFCs of an ordinary anisotropic material ε, μ and free space. b The EFCs of an artificial material with two equal-frequency surfaces (red and blue) shifted along the k_x and k_y directions, where external propagating photons can only excite the eigenstates with dispersions shifted along the k_x and k_y directions through red boundary α (BDY α) or blue boundary β (BDY β), respectively. c The eigenstates of the red or blue equal-frequency surface inside the artificial material are confined by the boundary β or boundary α due to the momentum mismatch. d Calculated band structure of artificial material I (AM I) for TE-polarization. The unit cell (inset) consists of an elliptical rod ($\varepsilon = 12$) with major

and minor axes of $0.8a$ and $0.5a$ in a host of $\varepsilon = 4$. a is the lattice constant. e The EFCs of the unit cell and supercells at the working frequency $fa/c = 0.25$ (dashed line in D). f Simulated electric field distributions, $\mathrm{Re}(E_z)$, for a point source illuminating a slab of artificial material I with α (left panel) or β (right panel) boundaries, respectively. The background is set as the corresponding effective medium ε_α, μ_α or ε_β, μ_β. The source is $10a$ away from the slabs, and the slab widths are $w = 6a$ and $w = 7a$, respectively. g Simulated electric intensity distributions ($|E_z|^2$), for a Gaussian beam incident upon the boundaries α (left panel) or β (right panel) of a square sample ($100a \times 100a$) of artificial material I, at 45°.

form of nonlocality[46,47] or effective gauge field[38–40] in the artificial material. Interestingly, when the momentum shift exceeds the range of the equal-frequency surface in free space, external propagating photons will selectively excite the eigenstates of the equal-frequency surfaces marked by red or blue in Fig. 2b through the α (red) or β (blue) boundaries, which correspond to the (1, 0) and (0, 1) lattice planes, respectively. Different sets of eigenstates lead to different effective optical parameters. More interestingly, inside the physical domain of the artificial material, the eigenstates of equal-frequency surfaces marked by red or blue are totally reflected at the mismatched boundary, i.e., β (blue) or α (red) boundary, due to momentum mismatch, as shown in Fig. 2c. This nonlocality-induced total reflection is only determined by the choice of eigenstates and regardless of the group velocity direction. Overall, the boundaries of artificial materials serve as the portals to excite different sets of eigenstates with dispersions shifted along different directions, corresponding to distinct optical effective media occupying the same space.

In the following, we demonstrate several practical designs of nonlocal artificial materials to construct two optical spaces with distinct refractive indices and impedances. The first design, artificial material I, is constructed using a square lattice of elliptical dielectric rods embedded in a dielectric host. The band structure for TE polarization is calculated and presented in Fig. 2d, with the unit cell shown in the inset. In the second band, around the working frequency $fa/c = 0.25$ (dashed line), there are two approximately elliptical equal-frequency surfaces shifted along the x (red) and y (blue) directions, as illustrated in the left panel of Fig. 2e. The constants of momentum shift are $k_\alpha = k_\beta = \pi/a$ in Eqs. 1a, b.

Because the unit cell of the artificial material is subwavelength ($a = \lambda/4$), the effective medium approximation is valid[48]. The effective parameters can be retrieved from the equal-frequency surface and effective impedance of the eigenstates of the artificial material[49]. The shift in momentum space introduces an additional phase difference[49] of $m\pi$ in transmission through an m-layer artificial material. When m is even, it is equivalent to consider the supercells consisting of two
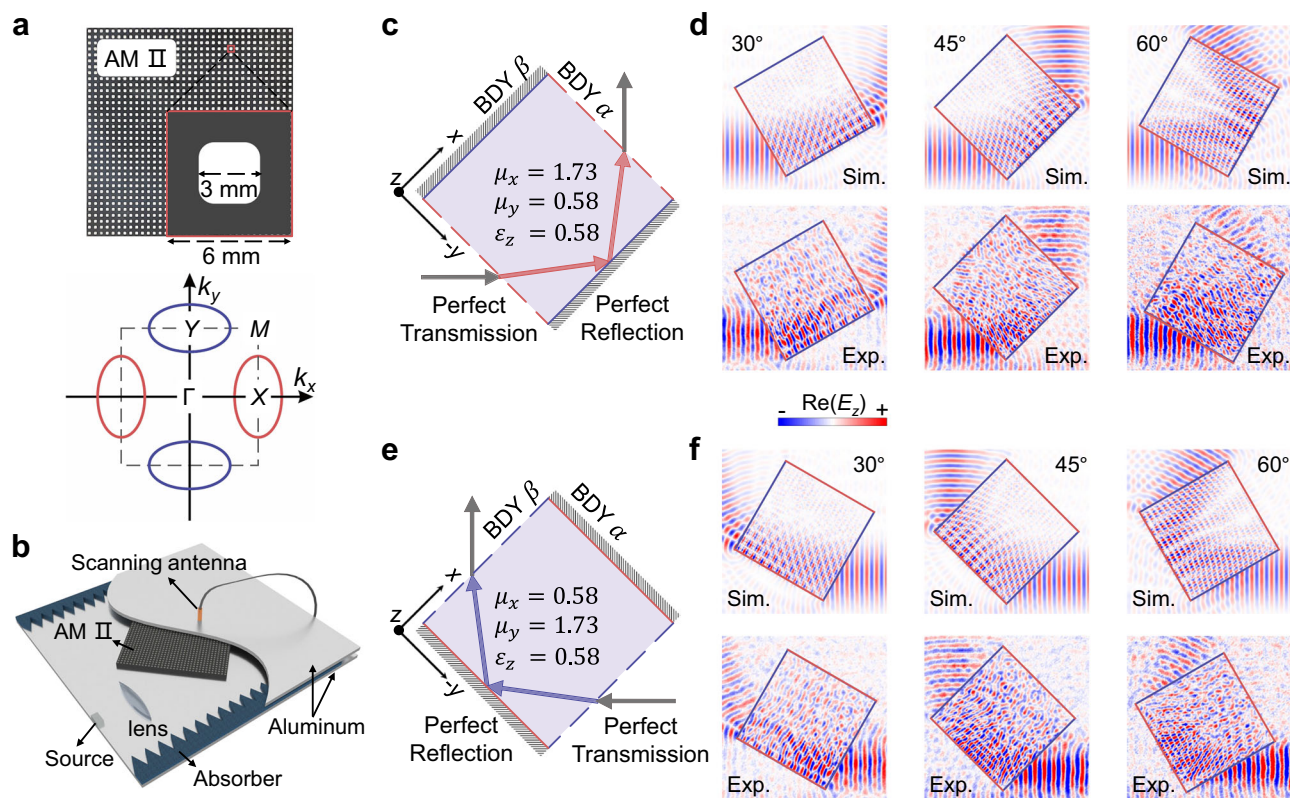
Fig. 3 | Experimental verification of photonic parallel spaces. a The photo of artificial material II (AM II) and its EFCs at the working frequency 14.75 GHz. The inset shows the unit cell, which consists of a square rod ($\varepsilon = 15.5$) of $0.5a \times 0.5a$ ($a = 6\ mm$) in a host material with $\varepsilon = 2.12$ and a fillet radius of $r = 0.75$ mm. The overall size of the sample is $35a \times 35a$. **b** The schematic diagram of the experimental setup. **c, e** Illustration of the conducted experiments. The red and blue arrows indicate different eigenstates excited through boundary α (BDY α) and boundary β (BDY β), respectively. **d, f** Simulated and experimental electric field distributions, Re(E_z), for the Gaussian beams incident on the boundary α (β) at 30°, 45°, and 60°, respectively.

original unit cells along the x or y direction (lattice constant is $2a$), such that the shifted dispersions are folded back to the Brillouin Zone center, as shown in the middle and right panels of Fig. 2e. This band folding yields a longer effective wavelength in the supercell picture. Then, effective parameters can be retrieved through the transmission and reflection coefficients[48] or the eigen-fields[49] (see Supplementary Note 1). Both methods lead to almost the same parameters. The retrieved effective parameters of artificial material I for boundaries α and β, i.e., $\boldsymbol{\varepsilon_\alpha}$, $\boldsymbol{\mu_\alpha}$, and $\boldsymbol{\varepsilon_\beta}$, $\boldsymbol{\mu_\beta}$, are $\mu_x^\alpha = 1.85$, $\mu_y^\alpha = 0.33$, $\varepsilon_z^\alpha = 1.12$, and $\mu_x^\beta = 0.40$, $\mu_y^\beta = 1.81$, $\varepsilon_z^\beta = 0.46$, respectively. We note that $\boldsymbol{\varepsilon_\alpha}$, $\boldsymbol{\mu_\alpha}$ (or $\boldsymbol{\varepsilon_\beta}$, $\boldsymbol{\mu_\beta}$) can only accurately describe the wave response of the bulk artificial material when external waves are incident upon the corresponding boundary α (or β), but cannot characterize the mismatched boundary β (or α). The effectiveness of these parameters is further verified by a large number of simulations (see Supplementary Note 2), confirming the efficacy over a wide range of incident angles. When m is odd, the effective parameters are still valid, except for an additional π phase in transmission, as shown in Supplementary Fig. 6.

We examine the validity of the effective parameters through full-wave simulations. In Fig. 2f, a point source is applied to illuminate a slab of artificial material I on either boundary α (left panel) or boundary β (right panel), in the corresponding background of $\boldsymbol{\varepsilon_\alpha}$, $\boldsymbol{\mu_\alpha}$, or $\boldsymbol{\varepsilon_\beta}$, $\boldsymbol{\mu_\beta}$, respectively. The absence of reflection and the matching wavefronts in transmission and incidence confirm the validity of the effective parameters. In the right panel, an additional π phase difference in transmission is caused by the odd number of layers. In Fig. 2g, we simulate the case of a Gaussian beam incident upon the boundary α (left panel) or β (right panel) of a square sample of artificial material I at 45°, from the background of $\boldsymbol{\varepsilon_\alpha}$, $\boldsymbol{\mu_\alpha}$, or $\boldsymbol{\varepsilon_\beta}$, $\boldsymbol{\mu_\beta}$, respectively. The intensity

distribution proves that the beam entering the artificial material from boundary α is totally reflected at boundary β, and vice versa. These simulations confirm the unique functions of material boundaries as portals to interact with different photonic parallel spaces characterized by distinct optical effective media.

The experimental verification of photonic parallel spaces

To experimentally verify the phenomenon of photonic parallel spaces, as well as the portal functions of the boundaries, we have designed and fabricated another artificial material (II) comprising a square array of square dielectric rods embedded in a dielectric host. Figure 3a shows a photo of the sample (upper panel) and the corresponding EFCs at the working frequency of 14.75 GHz (lower panel). The retrieved effective parameters for boundaries α and β are $\mu_x^\alpha = 1.73$, $\mu_y^\alpha = 0.58$, $\varepsilon_z^\alpha = 0.58$, and $\mu_x^\beta = 0.58$, $\mu_y^\beta = 1.73$, $\varepsilon_z^\beta = 0.58$, respectively, which satisfy omnidirectional impedance matching with free space[22], i.e., $\mu_x^\alpha \mu_y^\alpha \approx 1$, $\mu_x^\alpha \varepsilon_z^\alpha \approx 1$, and $\mu_x^\beta \mu_y^\beta \approx 1$, $\mu_x^\beta \varepsilon_z^\beta \approx 1$. This property ensures high transmittance through the boundaries α and β under almost all incident angles[22,49], as demonstrated in Supplementary Fig. 7. Figure 3b schematically illustrates the experimental setup, where artificial material II is placed inside a parallel-plate microwave waveguide. Gaussian beams are generated to impinge upon the boundaries α and β at 30°, 45°, and 60°. The electric field distribution is measured with a probing antenna. The frequency of measurement is set around 15.50 GHz, slightly above the designed frequency due to the influence of the small air gap between the artificial material and the upper aluminum plate for moving the antenna.

Figure 3c, e shows the illustrations of the performed experiments, where an external Gaussian beam is incident upon boundary α (β) at
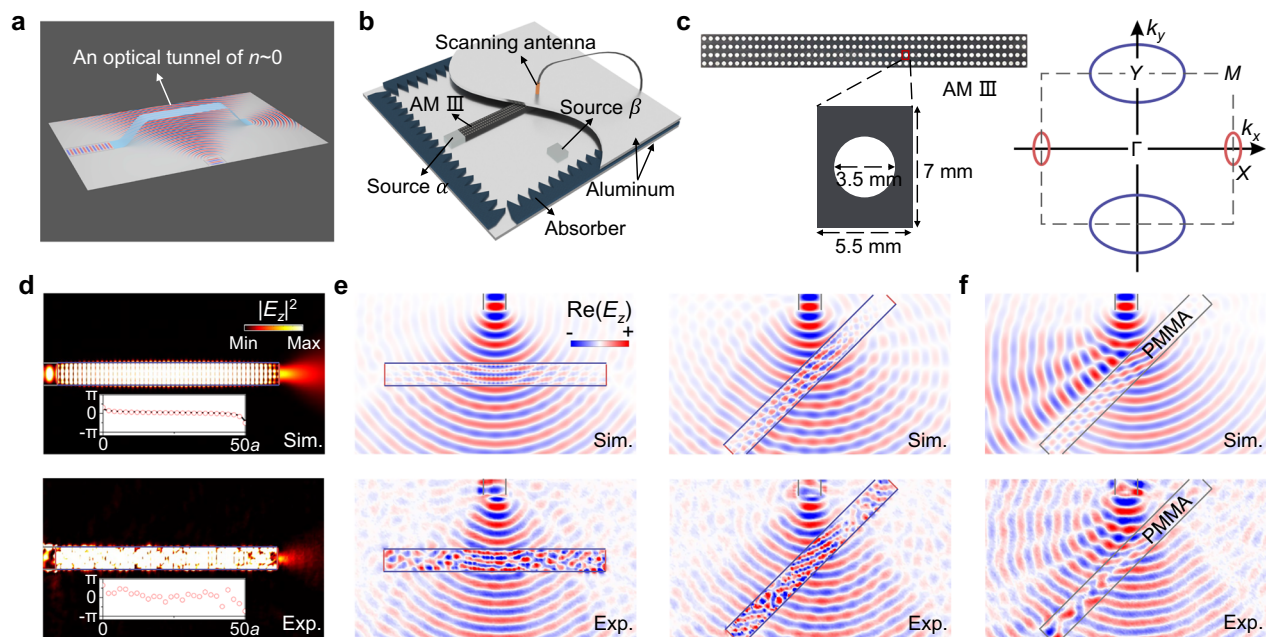
Fig. 4 | Experimental observation of a photonic wormhole. a The schematic diagram of an optical wormhole for a 2D plane. **b** The experimental setup. **c** Photo, unit cell and EFCs of artificial material III (AM III) ($50a \times 4b$) comprising a cylindrical rod ($\varepsilon = 15.5$) with a radius $r = 3.5$ mm in a dielectric host with $\varepsilon = 2.12$. The unit cell has the lattice constants of $a = 5.5$ mm and $b = 7$ mm. **d** Simulated and measured electric intensity distributions ($|E_z|^2$) for incident beams impinging upon boundary α (short side). The insets show the phase variations along the artificial material (red circles: simulation or experimental results, black solid lines: theoretical results). **e** Simulated and measured electric field distributions for incident beams incident upon boundary β (long side) at 0° and 45°. **f** Simulated and measured electric field distributions, Re(E_z), for incident beams incident upon the long boundary of a PMMA slab at 45°.

30°, 45°, and 60°. We expect the beam to completely transmit into the artificial material without any reflection, yet then totally reflect at the boundary β (α) inside the artificial material, irrespective of the incident angle. Figure 3d, f shows the simulated (upper panels) and measured (lower panels) electric field distributions. The omnidirectional impedance matching on different boundaries and total reflection inside the artificial material are clearly observed. The perfect matching between simulation and experimental results confirms the functions of photonic parallel spaces and material boundaries as portals. In the following, we demonstrate that photonic parallel spaces enable fascinating phenomena commonly believed to be possible only in higher-dimensional spaces.

Photonic wormholes as invisible optical tunnels

Wormholes are hypothetical tunnels in higher dimensions that cannot be detected in real space except at their throats (entrance and exit). The analogy of a wormhole for photons should have the ability to transport photons from one throat to the other with a shorter optical path, while maintaining invisible to other photons that have not entered the throats, as shown in Fig. 4a. Interestingly, this functionality can be realized by creating photonic parallel spaces with two specific optical spaces: one exhibiting an effective lower refractive index such that the optical path of the tunneling photons maintains short, and the other being omnidirectionally impedance-matched to free space such that reflection is totally eliminated.

We note that the effective refractive index, impedance, and anisotropy of the optical spaces can all be flexibly tailored by leveraging the rich degrees of freedom in the artificial material design (see Supplementary Note 4). Specifically, we have trained a deep neural network to precisely tune the properties of the two optical spaces. For instance, it is possible to keep one optical space almost fixed and only alter the other (see Supplementary Note 10). An artificial material III, with two optical spaces satisfying the conditions for photonic wormholes, is designed and fabricated. We note that the nonlocality-induced

internal reflection suppresses all modes below a cut-off frequency in finite-width channels, similar to metal waveguides for microwaves[34]. At this cut-off frequency, the effective refractive index approaches zero ($n \approx 0$)[34–37].

The experimental setup is illustrated in Fig. 4b, where the function of a long slab of artificial material III is investigated by scanning the electric field under excitation of different sources. Figure 4c depicts the photo of artificial material III, which comprises a rectangular array ($50a \times 4b$) of cylindrical dielectric rods embedded in a dielectric host. The long and short sides correspond to boundaries β and α, respectively. At the working frequency 13.38 GHz, the EFCs are shown in the right panel of Fig. 4c, confirming the large difference in the refractive indices of the two optical spaces. The retrieved effective parameters are $\mu_x^\alpha = 2.00$, $\mu_y^\alpha = 0.46$, $\varepsilon_z^\alpha = 0.057$ and $\mu_x^\beta = 0.61$, $\mu_y^\beta = 1.61$, $\varepsilon_z^\beta = 0.62$, respectively. Since $\mu_x^\beta \mu_y^\beta \approx 1$ and $\mu_y^\beta \varepsilon_z^\beta \approx 1$, the reflection is almost zero when the incident beams impinge upon boundary β (long side), regardless of the incident angle. Therefore, this artificial material slab is invisible in reflection. On the other hand, due to momentum mismatch, incident beams upon boundary α (short side) are totally confined to propagate along the slab. The cut-off frequency of boundary α is designed to match the working frequency of 13.38 GHz (see Supplementary Note 5), resulting in an effective epsilon-near-zero waveguide[34] with retrieved parameters of $\varepsilon_{eff} = 3.2 \times 10^{-3}$ and $\mu_{eff} = 0.48$. Here, the effective parameters are retrieved using the supercell of $2a$, as detailed in Supplementary Note 5. Despite the impedance mismatch, high transmittance can be conveniently achieved through Fabry-Pérot resonances.

Figure 4d presents the simulated and measured electrical field intensity distribution under incidence upon the boundary α. The air gap between artificial material III and the upper aluminum plate slightly increases the frequency of experimental measurement to around 14.10 GHz. Perfect wave confinement and guiding are clearly observed, proving the functionality of optical tunnels. The inset shows the slow phase variation of the electric field along the supercells of the

artificial material (see Supplementary Note 5), which is the signature of epsilon-near-zero waveguide[34]. This result implies a new strategy for suppressing radiation in pure dielectric epsilon-near-zero waveguides besides the bound states in the continuum method[50]. Figure 4e displays the calculated and measured electric field distributions under incidence upon the boundary β at 0° and 45°. Here, we omit the internal lattice details of artificial material III to maintain clarity in field maps. The sources are 80 mm away from the artificial material. The near-zero reflection confirms the impedance matching of the tunnel and it also applies to any other incident angles or location on boundary β (Supplementary Fig. 12). For comparison, substantial reflection is observed for a PMMA slab ($\varepsilon = 2.6$) under 45° incidence upon its long boundary, as clearly manifested by the electric field distribution in Fig. 4f. Fourier transformed spectra further support this conclusion, as shown in Supplementary Note 7.

A schematic graph demonstrating the general principle of realizing photonic wormholes is shown in Supplementary Fig. 14. Here, we note that the optical path and impedance of the tunnel can be flexibly tuned by changing the optical space associated with boundary α. With the aid of deep learning, it is possible to freely control the optical path experienced by the tunneling photons. Moreover, the functionality of such invisible optical tunnels is quite robust. In Supplementary Note 9, we introduce fluctuations in the rod sizes of the artificial material, but still observe excellent performances of invisibility and waveguiding.

Photonic multiple realities: optical devices operating in separate dimensions

Strikingly, more complicated designs of photonic parallel spaces enable two arbitrary optical devices or scatterers to share the same physical location yet function independently, as if existing in separate dimensions. Such a functionality is analogous to multiple realities or the multiverse for photons, but here we can realize it in practice. For demonstration, we design an artificial material as the coexistence of a boat-shaped scatterer and a tree-shaped scatterer, which will be independently experienced by the photons entering through different boundaries of the artificial material, as illustrated in Fig. 5a.

In this realization, four types of artificial material units (I-IV) are required and designed through deep learning (see Supplementary Note 10). When photons are incident upon the boundary α, units I and III are both characterized by ε_A, μ_A, while units II and IV are both characterized by ε_C, μ_C. Similarly, when photons are incident upon the boundary β, units I and II are both characterized by ε_B, μ_B, while units III and IV are both characterized by ε_D, μ_D. The retrieved effective parameters are $\mu_x = 1.93$, $\mu_y = 0.75$, $\varepsilon_z = 0.021$ for ε_A, μ_A, $\mu_x = 0.75$, $\mu_y = 1.93$, $\varepsilon_z = 0.021$ for ε_B, μ_B, $\mu_x = 1.89$, $\mu_y = 0.70$, $\varepsilon_z = 0.065$ for ε_C, μ_C and $\mu_x = 0.70$, $\mu_y = 1.89$, $\varepsilon_z = 0.065$ for ε_D, μ_D, respectively. Then, two inhomogeneous artificial materials, IV and V, are constructed using these four types of units, as depicted in Fig. 5b, c, respectively. In artificial material IV, unit II forms a boat-shaped scatterer. In artificial material V, the combined region of units II and IV forms a boat-shaped scatterer, while the combined region of units III and IV forms a tree-shaped scatterer. In both cases, Unit I is chosen as the background material.

Full-wave simulations are applied to validate the photonic multiple realities. The simulated setup is demonstrated in Supplementary Fig. 19. Figure 5d, e shows the simulated intensity distributions of the total electric field under the incidence of a Gaussian beam, for the cases of artificial materials IV and V, respectively. In Fig. 5d, it is seen that the boat-shaped scatterer exhibits a pronounced scattering effect under incidence upon boundary α, whereas negligible scattering is observed under incidence upon boundary β. This is because units I and II share almost the same effective parameters for boundary β. Similarly, units I and III in artificial material V exhibit almost the same effective parameters for boundary α, thus they are indistinguishable upon incidence at boundary α. In Fig. 5e, the scattering pattern is the same as

that of the boat-shaped scatterer upon incidence at boundary α, but it transitions to the scattering pattern of a tree-shaped scatterer upon incidence at boundary β. For comparison, the intensity distributions for the effective medium scatterers, i.e., a boat-shaped scatterer of ε_C, μ_C in a background of ε_A, μ_A, and a tree-shaped scatterer of ε_D, μ_D in a background of ε_B, μ_B, are also shown in Fig. 5f. It is observed that the scattering patterns of the artificial materials in Fig. 5d, e are indeed equivalent to those of the boat-shaped and tree-shaped scatterers. This feature is further confirmed by the quantitative analysis of electric-field amplitude along the boundaries in Supplementary Fig. 22. We emphasize that the optical response of the scatterer is solely determined by the boundary upon which external photons enter the artificial material and is independent of the incident direction. For instance, 30° (60°) incidence on boundary α and 60° (30°) incidence on boundary β refers to the same incident direction. These results confirm distinct optical devices coexisting at the same physical location, establishing photonic multiple realities with negligible crosstalk (see details in Supplementary Fig. 23).

The optical devices or scatterers created in two optical spaces can be almost arbitrary, thus this approach opens immense degrees of freedom in designing multiple-realities optical devices. As another example, a convex lens and a concave lens are created in a single artificial material and operate independently, as shown in Supplementary Fig. 20. Similarly, a plethora of previously unthinkable multiple-realities functions can be realized in practice, as shown in Supplementary Fig. 21.

Discussion

Previous implementations of multi-functionality have mostly relied on multiplexing based on polarization[51,52], frequency[53,54], space[54,55], or angular momentum[56,57], etc. Here, our approach has opened a new degree of freedom, i.e., nonlocality, which enables boundary-determined optical spaces for multiplexing. The number of independent optical spaces is determined by the lattice type, which defines the number of Brillouin zone edge pairs. More optical spaces can be achieved by using higher-symmetry lattices, such as the triangular or cubic structures, offering potential for even greater capacity. Meanwhile, the nonlocal artificial materials support seamless scalability to IR/visible regimes, as they primarily consist of low-loss dielectric structures. These structures are not only available at optical frequencies but also compatible with mature nanofabrication techniques. Photonic parallel spaces for other polarizations and combined with traditional degrees of freedom, have also been designed (Supplementary Note 4). The working bandwidth of this phenomenon depends on the frequency range of multiple shifted dispersions, which in principle could be extended to a wide spectrum[40].

The unit cells of the artificial materials utilized here are at an intermediate scale between those of metamaterials[5–8] and photonic-band-gap materials[9]. At this scale, higher-order diffraction remains absent, allowing an accurate effective-medium description, but equal-frequency surfaces are shifted to locate near Brillouin zone boundaries. Such a specific form of nonlocality has previously enabled intriguing phenomena such as all-angle transparency[49] and complete removal of claddings in waveguiding systems[58]. Here, we point out that supercell-induced band folding could map these surfaces back to the Brillouin zone center, making a local effective-medium description applicable to waves incident upon specific boundaries. This treatment not only preserves the validity of the effective-medium approximation but also introduces the unique feature of boundary-selective parallel spaces. Another fundamental difference with previous works focusing on a single shifted equal-frequency surface[38,39,49,58] is the coexistence of multiple equal-frequency surfaces shifted along different directions, which is the key to realizing photonic parallel spaces.

The parallel spaces demonstrated here can also be viewed as a special form of illusion or camouflage effects[22–33]. Previous
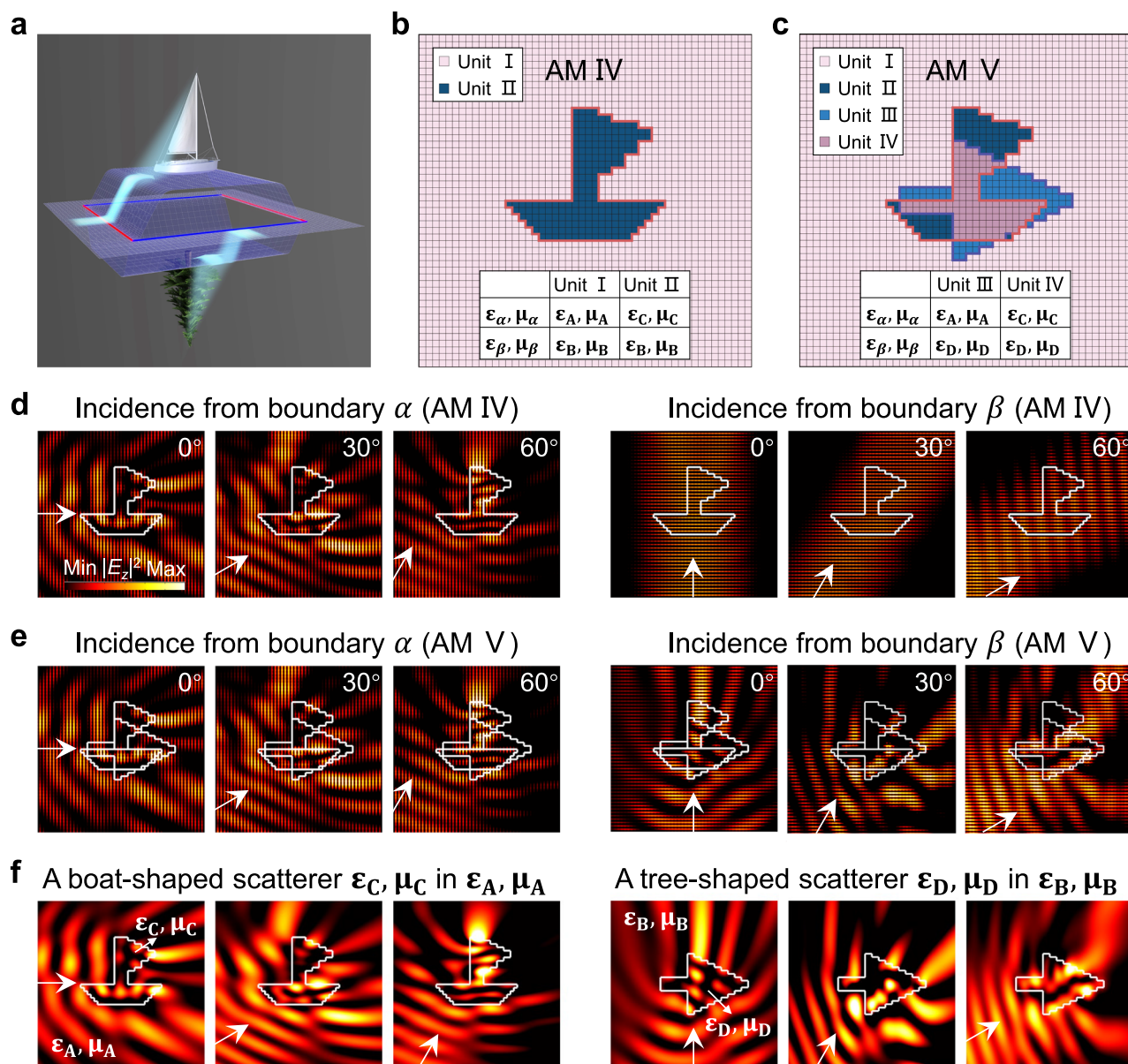
Fig. 5 | Photonic multiple realities. a Schematic picture of two optical spaces containing a boat-shaped scatterer and a tree-shaped scatterer. **b, c** The configurations of artificial materials IV and V (AM IV and AM V) consist of four types of units. The inset tables show the effective parameters associated with these units. **d, e** The intensity distributions ($|E_z|^2$) for artificial materials IV and V under the incidence of a Gaussian beam upon boundaries α and β at 0°, 30°, and 60°. **f** The intensity distributions for effective medium scatterers, i.e., boat-shaped scatterer of ε_C, μ_C in a background of ε_A, μ_A, and tree-shaped scatterer of ε_D, μ_D in a background of ε_B, μ_B, under the incidence of a Gaussian beam at 0°, 30°, and 60°.

investigations based on transformation optics and recent advances, such as the merging of diffuse reflection and transparency[30–32] and ultra-broadband cloaking illusion[33] have shown exceptional abilities to create illusions with metamaterials. However, our findings here manifest the feasibility of emulating separate dimensions for the first time, thereby extending the scope of illusion or camouflage optics to the field of high-dimensional physics, which has recently seen extensive investigations through various methods like topological pumping[59], connectivity[60], and synthetic dimensions[41,42]. Here, the boundaries of physical space are leveraged as the crucial parameters for constructing a new dimension beyond the actual physical domain. Such boundaries, serving as portals to access different optical spaces with distinct properties and functionalities, function as optical analogs of the magical wardrobe in "The Lion, the Witch, and the Wardrobe."

Our current designs are fixed during fabrication. But if active materials, such as liquid crystals[61], phase-change materials[62], electro-optic/thermo-optic materials[63,64], or PIN diodes[65], are incorporated in the system, dynamic modulation of photonic parallel spaces could also be allowed in the future.

Our discovery offers a new route to overcoming key limitations of optical devices, such as bulky designs, limited functionality, and susceptibility to interference in complex environments. It may turbo-charge the development of integrated photonics[66,67], where scientists continually pack more functional devices into shrinking footprints. The universality of this methodology enables extension to diverse wave systems, including phononic, plasmonic, and even electronic waves. Therefore, this breakthrough heralds a new era for creating multifunctional materials and devices that effectively transcend their dimensional constraints.

Methods

Calculations and simulations

The numerical calculations, encompassing band structure calculation, eigenstate analysis, along wave simulations, are carried out using the finite-element software COMSOL Multiphysics. All eigenstates and band structures are calculated within a 2D unit cell, utilizing Floquet periodic boundary conditions along the two lattice vectors. Full-wave simulations were performed in the frequency domain, employing ports to introduce Gaussian beams and mode sources. Transmittances are obtained from the S parameters of these ports, and Floquet periodic boundary conditions are applied to the top and bottom boundaries to accurately simulate the behavior of slabs.

Experimental setup

In the microwave experiments, the artificial optical material, comprising hydrocarbon resin mixed with ceramic rods in a PTFE host, is placed within a parallel-plate waveguide formed by two flat aluminum plates. The plates are separated by 8 mm, matching the height of the material and ensuring the separation is less than half the wavelength of interest (20 mm for 15 GHz). This configuration ensures that the waveguide supports only transverse electromagnetic modes. Gaussian beams are generated using a combination of the waveguide and a lens. The electric field distribution is probed by a miniature antenna inserted through a small, insulated hole in the upper plate; only 1 mm of its 1 mm diameter tip extends into the measurement region, minimizing perturbation. This probing antenna is mounted on a stepper motor. The emitting waveguide source and the probing antenna are connected to a KEYSIGHT N5224B network analyzer (VNA), on which a standard SOLT (short–open–load–through) calibration was performed at each port to eliminate cable and connector dispersion, ensure flat amplitude response, and establish an accurate phase reference across the band. To suppress residual probe loading, 20 repeated S-parameter measurements were averaged at each point under enhanced output power and narrow filter bandwidth. Mechanical alignment of the plates to micrometer-level parallelism further guaranteed uniform air gap thickness during scanning. Finally, because the single-scan measurement area (250 mm × 250 mm) was not large enough to cover the entire sample and surrounding fields, the overall field maps were obtained by stitching together multiple adjacent scans.

Data availability

All data supporting the findings of this study are provided within the paper and the Supplementary Information. The raw experimental datasets generated in this study are provided in the Source Data file. Source data are provided with this paper.

Code availability

The source code, datasets, and models generated in this study for both forward neural network training and inverse design are provided in the Supplementary Information.

References

1. Tegmark, M. *Our Mathematical Universe: My Quest for the Ultimate Nature of Reality* (Vintage, 2014).
2. Einstein, A. & Rosen, N. The particle problem in the general theory of relativity. *Phys. Rev.* **48**, 73–77 (1935).
3. Hawking, S. W. Quantum coherence down the wormhole. *Phys. Lett. B* **195**, 337–343 (1987).
4. Jafferis, D. et al. Traversable wormhole dynamics on a quantum processor. *Nature* **612**, 51–55 (2022).
5. Smith, D. R., Pendry, J. B. & Wiltshire, M. C. K. Metamaterials and negative refractive index. *Science* **305**, 788–792 (2004).
6. Liu, Y. & Zhang, X. Metamaterials: a new frontier of science and technology. *Chem. Soc. Rev.* **40**, 2494–2507 (2011).
7. Poddubny, A., Iorsh, I., Belov, P. & Kivshar, Y. Hyperbolic metamaterials. *Nat. Photonics* **7**, 948–957 (2013).
8. Jahani, S. & Jacob, Z. All-dielectric metamaterials. *Nat. Nanotechnol.* **11**, 23–36 (2016).
9. Joannopoulos, J. D., Johnson, S. G., Winn, J. N. & Meade, R. D. *Photonic Crystals: Molding the Flow of Light* 2nd edn (Princeton University Press, 2011).
10. Joannopoulos, J. D., Villeneuve, P. R. & Fan, S. Photonic crystals: putting a new twist on light. *Nature* **386**, 143–149 (1997).
11. Yablonovitch, E. Inhibited Spontaneous Emission in Solid-State Physics and Electronics. *Phys. Rev. Lett.* **58**, 2059–2062 (1987).
12. John, S. Strong localization of photons in certain disordered dielectric superlattices. *Phys. Rev. Lett.* **58**, 2486–2489 (1987).
13. Lu, L., Joannopoulos, J. D. & Soljačić, M. Topological photonics. *Nat. Photonics* **8**, 821–829 (2014).
14. Ozawa, T. et al. Topological photonics. *Rev. Mod. Phys.* **91**, 015006 (2019).
15. Chen, Y. et al. Observation of intrinsic chiral bound states in the continuum. *Nature* **613**, 474–478 (2023).
16. Kang, M., Liu, T., Chan, C. T. & Xiao, M. Applications of bound states in the continuum in photonics. *Nat. Rev. Phys.* **5**, 659–678 (2023).
17. Wang, B. et al. Generating optical vortex beams by momentum-space polarization vortices centred at bound states in the continuum. *Nat. Photonics* **14**, 623–628 (2020).
18. Jin, J. et al. Topologically enabled ultrahigh-Q guided resonances robust to out-of-plane scattering. *Nature* **574**, 501–504 (2019).
19. Pendry, J. B. Negative refraction makes a perfect lens. *Phys. Rev. Lett.* **85**, 3966–3969 (2000).
20. Fang, N., Lee, H., Sun, C. & Zhang, X. Sub-diffraction-limited optical imaging with a silver superlens. *Science* **308**, 534–537 (2005).
21. Guan, F. et al. Overcoming losses in superlenses with synthetic waves of complex frequency. *Science* **381**, 766–771 (2023).
22. Pendry, J. B., Schurig, D. & Smith, D. R. Controlling electromagnetic fields. *Science* **312**, 1780–1782 (2006).
23. Leonhardt, U. Optical conformal mapping. *Science* **312**, 1777–1780 (2006).
24. Pendry, J. B., Luo, Y. & Zhao, R. Transforming the optical landscape. *Science* **348**, 521–524 (2015).
25. Valentine, J., Li, J., Zentgraf, T., Bartal, G. & Zhang, X. An optical cloak made of dielectrics. *Nat. Mater.* **8**, 568–571 (2009).
26. Lai, Y. et al. Illusion optics: the optical transformation of an object into another object. *Phys. Rev. Lett.* **102**, 253902 (2009).
27. Greenleaf, A., Kurylev, Y., Lassas, M. & Uhlmann, G. Electromagnetic wormholes and virtual magnetic monopoles from metamaterials. *Phys. Rev. Lett.* **99**, 183901 (2007).
28. Zhu, J., Liu, Y., Liang, Z., Chen, T. & Li, J. Elastic waves in curved space: mimicking a wormhole. *Phys. Rev. Lett.* **121**, 234301 (2018).
29. Qian, C. et al. Deep-learning-enabled self-adaptive microwave cloak without human intervention. *Nat. Photonics* **14**, 383–390 (2020).
30. Chu, H. et al. Diffuse reflection and reciprocity-protected transmission via a random-flip metasurface. *Sci. Adv.* **7**, eabj0935 (2021).
31. Chu, H. et al. Matte surfaces with broadband transparency enabled by highly asymmetric diffusion of white light. *Sci. Adv.* **10**, eadm8061 (2024).
32. Shi, J. et al. Parity metamaterials and dynamic acoustic mimicry. *Research* **8**, 0826 (2025).
33. Liu, C., Ma, C., Lai, Y. & Fang, N. X. Ultra-broadband illusion acoustics for space and time camouflages. *Nat. Commun.* **15**, 8046 (2024).
34. Edwards, B., Alù, A., Young, M. E., Silveirinha, M. & Engheta, N. Experimental verification of epsilon-near-zero metamaterial coupling and energy squeezing using a microwave waveguide. *Phys. Rev. Lett.* **100**, 033903 (2008).

35. Huang, X., Lai, Y., Hang, Z. H., Zheng, H. & Chan, C. T. Dirac cones induced by accidental degeneracy in photonic crystals and zero-refractive-index materials. *Nat. Mater.* **10**, 582–586 (2011).

36. Li, Y. et al. On-chip zero-index metamaterials. *Nat. Photonics* **9**, 738–742 (2015).

37. Liberal, I. & Engheta, N. Near-zero refractive index photonics. *Nat. Photonics* **11**, 149–158 (2017).

38. Fang, K. & Fan, S. Controlling the flow of light using the inhomogeneous effective gauge field that emerges from dynamic modulation. *Phys. Rev. Lett.* **111**, 203901 (2013).

39. Lumer, Y. et al. Light guiding by artificial gauge fields. *Nat. Photonics* **13**, 339–345 (2019).

40. Chen, W.-J., Hou, B., Zhang, Z.-Q., Pendry, J. B. & Chan, C. T. Metamaterials with index ellipsoids at arbitrary k-points. *Nat. Commun.* **9**, 2086 (2018).

41. Lustig, E. et al. Photonic topological insulator in synthetic dimensions. *Nature* **567**, 356–360 (2019).

42. Dutt, A. et al. A single photonic cavity with two independent physical synthetic dimensions. *Science* **367**, 59–64 (2020).

43. Smolyaninov, I. I. Metamaterial 'multiverse. *J. Opt.* **13**, 024004 (2011).

44. Smolyaninov, I. I., Yost, B., Bates, E. & Smolyaninova, V. N. Experimental demonstration of metamaterial "multiverse" in a ferrofluid. *Opt. Express* **21**, 14918–14925 (2013).

45. Ma, W. et al. Deep learning for the design of photonic structures. *Nat. Photonics* **15**, 77–90 (2021).

46. Malek, S. C., Overvig, A. C., Alù, A. & Yu, N. Multifunctional resonant wavefront-shaping meta-optics based on multilayer and multi-perturbation nonlocal metasurfaces. *Light Sci. Appl.* **11**, 246 (2022).

47. Shastri, K. & Monticone, F. Nonlocal flat optics. *Nat. Photonics* **17**, 36–47 (2023).

48. Smith, D. R., Schultz, S., Markoš, P. & Soukoulis, C. M. Determination of effective permittivity and permeability of metamaterials from reflection and transmission coefficients. *Phys. Rev. B* **65**, 195104 (2002).

49. Luo, J. et al. Ultratransparent media and transformation optics with shifted spatial dispersions. *Phys. Rev. Lett.* **117**, 223901 (2016).

50. Dong, T. et al. Low-loss nanoscale zero-index metawaveguides and metadevices. *Optica* **11**, 799–805 (2024).

51. Danner, A. J., Tyc, T. & Leonhardt, U. Controlling birefringence in dielectrics. *Nat. Photonics* **5**, 357–359 (2011).

52. Smolyaninova, V. N., Ermer, H. K., Piazza, A., Schaefer, D. & Smolyaninov, I. I. Experimental demonstration of birefrigent transformation optics devices. *Phys. Rev. B* **87**, 075406 (2013).

53. Marin-Palomo, P. et al. Microresonator-based solitons for massively parallel coherent optical communications. *Nature* **546**, 274–279 (2017).

54. Zhang, L. et al. A wireless communication scheme based on space- and frequency-division multiplexing using digital metasurfaces. *Nat. Electron.* **4**, 218–227 (2021).

55. Puttnam, B. J., Rademacher, G. & Luís, R. S. Space-division multiplexing for optical fiber communications. *Optica* **8**, 1186–1203 (2021).

56. Willner, A. E., Pang, K., Song, H., Zou, K. & Zhou, H. Orbital angular momentum of light for communications. *Appl. Phys. Rev.* **8**, 041312 (2021).

57. Wang, J. et al. Orbital angular momentum and beyond in free-space optical communications. *Nanophotonics* **11**, 645–680 (2022).

58. Song, T. et al. Ultracompact photonic circuits without cladding layers. *Phys. Rev. X* **12**, 011053 (2022).

59. Zilberberg, O. et al. Photonic topological boundary pumping as a probe of 4D quantum Hall physics. *Nature* **553**, 59–62 (2018).

60. Wang, Y., Price, H. M., Zhang, B. & Chong, Y. D. Circuit implementation of a four-dimensional topological insulator. *Nat. Commun.* **11**, 2356 (2020).

61. Chen, P., Wei, B.-Y., Hu, W. & Lu, Y.-Q. Liquid-crystal-mediated geometric phase: from transmissive to broadband reflective planar optics. *Adv. Mater.* **32**, 1903665 (2020).

62. Wuttig, M., Bhaskaran, H. & Taubner, T. Phase-change materials for non-volatile photonic applications. *Nat. Photonics* **11**, 465–476 (2017).

63. Rahmani, M. et al. Reversible thermal tuning of all-dielectric metasurfaces. *Adv. Funct. Mater.* **27**, 1700580 (2017).

64. Qi, Y. & Li, Y. Integrated lithium niobate photonics. *Nanophotonics* **9**, 1287–1320 (2020).

65. Feng, Y. et al. Reconfigurable intelligent surfaces: design, implementation, and practical demonstration. *Electromagn. Sci.* **1**, 1–21 (2023).

66. Cheben, P., Halir, R., Schmid, J. H., Atwater, H. A. & Smith, D. R. Subwavelength integrated photonics. *Nature* **560**, 565–572 (2018).

67. Marpaung, D., Yao, J. & Capmany, J. Integrated microwave photonics. *Nat. Photonics* **13**, 80–90 (2019).

Acknowledgements

Author contributions

Y. Lai conceived the idea and concept. T.T. Song performed the theoretical designs and numerical simulations. Y.X. Jing performed design and simulation in deep learning. C.H. Shen and H.C. Chu performed the microwave measurements. J. Luo, R.Q. Jia, C. Wang, M. Xiao, and Z.Q. Zhang helped in the analysis and discussions. Y. Lai, C.T. Chan, R.W. Peng, and M. Wang organized and led the project. All authors contributed to the writing of the manuscript.

Competing interests

The authors declare no competing interests.

Additional information

Supplementary information The online version contains supplementary material available at https://doi.org/10.1038/s41467-025-63981-3.

Correspondence and requests for materials should be addressed to Ruwen Peng, Mu Wang, C. T. Chan or Yun Lai.

Peer review information *Nature Communications* thanks Viktoriia Rutckaia and the other, anonymous, reviewers for their contribution to the peer review of this work. A peer review file is available.

Reprints and permissions information is available at http://www.nature.com/reprints